

Crossed Andreev reflection in altermagnets

Sachchidanand Das¹ and Abhiram Soori^{1,*}

¹*School of Physics, University of Hyderabad, Prof. C. R. Rao Road, Gachibowli, Hyderabad-500046, India*

Crossed Andreev reflection (CAR) is a scattering phenomenon occurring in a superconductor (SC) connected to two metallic leads, where an incident electron on one side of the SC emerges on the opposite side as a hole. Despite its significance, CAR detection is often impeded by the prevalent electron tunneling (ET), wherein the incident electron exits on the opposing side as an electron. One approach to augment CAR over ET involves employing two antiparallel ferromagnets across the SC. However, this method is constrained by the low polarization in ferromagnets and necessitates the application of a magnetic field. Altermagnets (AMs) present a promising avenue for detecting and enhancing CAR due to their distinct Fermi surfaces for the two spins. Here, we propose a configuration utilizing two AMs rotated by 90° with respect to each other on either side of an SC to enhance CAR. We calculate local and nonlocal conductivities across the AM-SC-AM junction using the Landauer-Büttiker scattering approach. Our findings reveal that in the strong phase of AMs, CAR overwhelmingly dominates nonlocal transport. In the weak phase, CAR can exhibit significant enhancement for larger values of the altermagnetic parameter compared to the scenario where AMs are in the normal metallic phase. As a function of the length of the SC, the conductivities exhibit oscillations reminiscent of Fabry-Pérot interference.

I. INTRODUCTION

Electrons are characterized by charge and spin. While the charge of the electrons is a characteristic used in electronics, their spin is the characteristic which has opened up a new field of study known as spintronics¹⁻⁷. Ferromagnets and antiferromagnets have played a central role in spintronics so far³. In ferromagnets, a majority of spins are aligned in one direction, resulting in a net spin polarization. On the other hand, in antiferromagnets neighboring spins point in opposite direction, making the net spin polarization zero. Recently, a new class of magnetic materials known as AMs have generated interest among theorists and experimentalists⁸⁻¹⁵. In AMs, the dispersions of the two spin sectors are separated in momentum space while maintaining a zero net spin polarization. In contrast to spin-orbit coupled systems, time reversal symmetry is broken in AMs. A consequence of such feature is that even though the net spin polarization is zero in both: a metal and an AM, a junction between the two carries a net spin current on application of a voltage bias¹⁶. Even before AMs were introduced, the concept of spin split bandstructures as in AMs was explored in literature^{17,18}. It has been predicted that some antiferromagnets can be turned into AMs by application of electric field¹⁹.

Even in ferromagnetic metals (FMs), the dispersions for the two spins are separated, but with a net spin polarization. This property enables the use of FMs in detecting crossed Andreev reflection (CAR)²⁰ - a phenomenon wherein an electron incident onto a SC from a FM gets transmitted into another FM as a hole. Enhancement of CAR is important from the point of view of developing quantum devices that use non-locally entangled electrons. Cooper pairs in singlet SC are entangled. Cooper pair splitting (CPS) is a process which separates the two electrons of a Cooper pair into two metals connected to the SC, maintaining their entanglement²¹⁻²³. CPS hap-

pens when current is driven from SC into two connected metals, whereas CAR happens when the current is driven from one of the two metals into the SC. Hence, CPS is the inverse process of CAR and enhancing CAR in a setup can result in an enhanced CPS in the same setup when the current is driven from SC to the two metals.

Hindrance to experimental observation of CAR is rooted in a competing process known as electron tunneling (ET) in which the electron transmits across the SC from one metal onto the other metal as an electron. The currents carried by ET and CAR are opposite in sign and in most cases, the current carried by ET overpowers the current carried by CAR and masks the signature of CAR²⁴. Several proposals have been put forward to circumvent this limitation and enhance CAR over ET²⁵⁻³², of which two methods have been implemented experimentally^{20,33} including the one where two antiparallel FMs are used. The use of FMs typically requires application of magnetic fields in experiments^{20,34}. Antiparallel alignment of ferromagnetic electrodes requires an external field, carefully stabilized in a particular field region³⁵. In devices that comprise CAR based components, applying magnetic field will affect the functioning of other components. Effect of ferromagnetic components along with external magnetic field can cause significant effects due to spurious fringing fields³⁶, which need to be eliminated - hence absence of external magnetic field/ FMs is an advantage. While a magnetic field of the order of 20mT is needed to get the FMs antiparallel²⁰, a magnetic field of the order of 0.1mT is sufficient to give rise to an effect such as superconducting diode effect³⁶. AMs provide an edge over FMs, because they require no external field for such alignment¹⁰.

AMs have been predicted to affect the superconducting transition temperature when coupled with SCs³⁷. In this work³⁷, SC sandwiched between two AMs in two possible configurations is studied: the two AMs are parallel, and the two AMs are rotated by 90° with respect to one

another. The superconducting transition temperature is found to be lower in the latter configuration compared to that in the former. The authors claim that this is due to enhanced CPS (inverse CAR) in the latter configuration, which favors the Cooper pairs to be broken into electrons. The idea that CAR is enhanced when the two AMs rotated with respect to one another are connected to an SC is worth an in-detail investigation. Also, Josephson effect that depends on the crystallographic orientation in SC-AM-SC junctions have been studied recently^{38–40}.

In this work, we study transport across an AM-SC-AM junction. We find that CAR is enhanced for certain crystallographic orientations of AMs. For AMs in the strong phase, ET can be completely suppressed, making way for CAR to solely dominate the nonlocal transport.

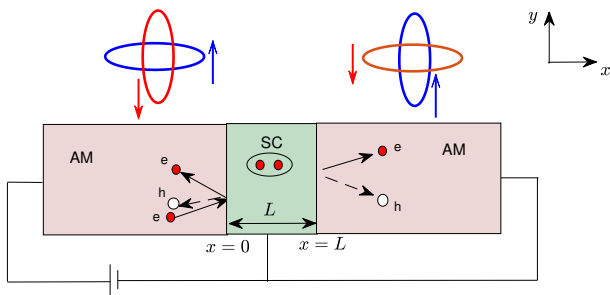


FIG. 1. Schematic of the setup. An s-wave SC is sandwiched between two AMs that are rotated by 90° with respect to each other. Bias is applied from the left AM, maintaining the SC and the right AM grounded. An electron incident from the left AM onto SC can reflect either as an electron or as a hole, or transmit through SC and emerge onto the right AM as an electron or as a hole.

II. SET-UP

The Hamiltonian for an AM is given by

$$H_{\vec{k}} = -2t_0(\cos k_x a + \cos k_y a)\sigma_0 + 2t_J(\cos k_x a - \cos k_y a)\sigma_z - \mu, \quad (1)$$

where t_J is the spin and direction dependent hopping which characterizes the altermagnetic phase, t_0 is the

hopping, a is the lattice spacing and σ_0 , σ_z are identity- and Pauli spin matrices. While most AMs are insulating, in this work by AM, we mean altermagnetic metals. In an earlier work¹⁶, we classified AMs into strong- or weak- phase depending upon whether $t_J > t_0$ or $t_J < t_0$. We stick to this convention for convenience. RuO_2 is an example for AM in the weak phase¹⁰ while Mn_5Si_3 is possibly an example for AM in the strong phase⁴¹. We consider an AM-SC-AM junction arranged in such a way that the AM on the right is rotated by 90° with respect to the AM on the left, as shown in Fig. 1. We shall see that this helps in enhancing CAR. A bias is applied from the left AM, keeping the SC and the right AM grounded. We calculate the local conductivity $G_{LL} = dI_L/dV$ and the nonlocal conductivity $G_{RL} = dI_R/dV$, where V is the bias, I_L (I_R) is the current density in the left (right) AM, by Landauer-Büttiker approach^{27,42,43}.

III. ALTERMAGNETS IN THE STRONG PHASE

In this section, we consider the AMs to be in the strong phase by choosing $t_0 = 0$, $t_J > 0$. This choice of parameters captures the essential physics of the setup in the strong phase of AMs and is not motivated by the experimental values of the parameters. The Hamiltonian for the AM on the left is obtained by expanding the Hamiltonian in eq. 1 around the band bottom. The band bottoms for the two spins are located at different points in the Brillouin zone. For the AM on the left, the band bottom for \uparrow (\downarrow)-spin is at $(\pm\pi/a, 0)$ [$(0, \pm\pi/a)$]. The Hamiltonian in the superconducting region mixes \uparrow (\downarrow)-spin electron with \downarrow (\uparrow)-spin hole. σ_z commutes with the full Hamiltonian. Hence, we can work in the two sectors: (i) \uparrow -spin electron- \downarrow -spin hole [\uparrow_e, \downarrow_h], and (ii) \downarrow -spin electron- \uparrow -spin hole [\downarrow_e, \uparrow_h] separately.

A. (\uparrow_e, \downarrow_h) sector

In the sector (i), the Hamiltonian can be written as $\sum_{\vec{k}} \Psi_{\vec{k}}^\dagger H_{\vec{k}} \Psi_{\vec{k}}$, where $\Psi_{\vec{k}} = [c_{\uparrow, k}, c_{\downarrow, -k}^\dagger]^T$ and

$$H_{\vec{k}} = \begin{cases} [t_J((k_x a \pm \pi)^2 + k_y^2 a^2) - \mu] \frac{\tau_z + \tau_0}{2} + [t_J(k_x^2 a^2 + (k_y a \pm \pi)^2) - \mu] \frac{\tau_z - \tau_0}{2}, & \text{for } x < 0, \\ \left[\frac{\hbar^2 (k_x^2 + k_y^2)}{2m} - \mu_s \right] \tau_z + \Delta \tau_x, & \text{for } 0 < x < L, \\ [t_J((k_x a \pm \pi)^2 + k_y^2 a^2) - \mu] \frac{\tau_z - \tau_0}{2} + [t_J(k_x^2 a^2 + (k_y a \pm \pi)^2) - \mu] \frac{\tau_z + \tau_0}{2}, & \text{for } x > L, \end{cases} \quad (2)$$

where τ_j , for $j = 0, x, z$ are the Pauli spin matrices acting

on the particle-hole sector, Δ is the superconducting gap,

and $c_{\vec{k},\sigma}$ annihilates an electron with wave vector \vec{k} and spin σ . In eq. (2), the AM Hamiltonian is expanded around $k_x = \pm\pi/a$ and $k_y = \pm\pi/a$. When the range of k_x (k_y) is taken to be $[-\pi/a, \pi/a]$, the Hamiltonian is expanded about $k_x = \pi/a$ ($k_y = \pi/a$) for positive k_x (k_y) and about $k_x = -\pi/a$ ($k_y = -\pi/a$) for negative k_x (k_y).

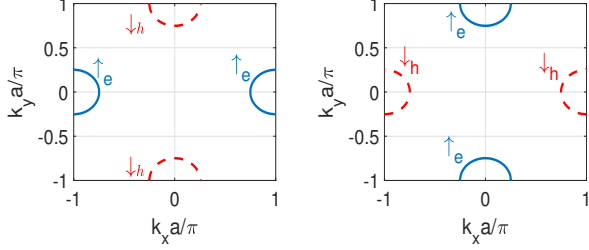


FIG. 2. Schematic of the Fermi surfaces of AMs on the left and the right in the strong phase. Blue solid line shows \uparrow_e and red dashed line shows \downarrow_h .

Four processes can occur when an electron is incident on the AM-SC-AM junction from the left AM. The electron with same spin can get reflected [electron reflection (ER)] or a hole with opposite spin can get reflected [Andreev reflection (AR)]⁴⁴ or an electron with same spin can transmit to the other AM [electron tunneling (ET)] or a hole with opposite spin can transmit to the other AM [crossed Andreev reflection (CAR)]^{20,24}. Conservation of probability current density along x -direction results in a competition among the four processes. Suppression of any one of them is balanced by enhancement in other processes. Since the system is translationally invariant along y -direction, matching or mismatching of k_y in the dispersion relations on different sides determines which of the above phenomena is more likely to occur. For instance, we can see that in Fig. 2, for \uparrow -spin electron incident from the left AM with a particular k_y , there exists \downarrow -spin hole on the right AM with same k_y , but there exists no \uparrow -spin electron states with the same k_y on the right AM. But k_y has to be the same for all the states in the two regions. This means that while the k_x corresponding to the \downarrow -spin hole is real, k_x corresponding to the \uparrow -spin electron is complex on the right AM. Since the states with real k_x carry current and the states with complex k_x carry no current, current on the right AM is carried by \downarrow -spin holes alone.

If on the right side, the crystallographic orientation of the AM is same as that on the left side, then for k_y of incident up-spin electrons, and that of down-spin hole on the right AM do not match, which means CAR is not possible. But k_y values for the up-spin electrons on the left and the right AM regions match, resulting ET. Therefore, we notice that if we take two strong AMs whose crystallographic orientations are the same on the two sides of a SC, CAR does not occur. When the two AMs are oriented at 90° to each other, CAR happens, but not ET.

The eigenstates in AM regions are either purely

electron-like or purely hole-like. The energy eigenvalues in the left AM for \uparrow_e and \downarrow_h are $E_{e,\uparrow} = t_J[(k_{ex}a - \pi)^2 + k_{ey}^2 a^2] - \mu$ and $E_{h,\downarrow} = -t_J[k_{hx}^2 a^2 + (k_{hy}a \pm \pi)^2] + \mu$ respectively. The eigenvectors for \uparrow_e and \downarrow_h are $[1, 0]^T$ and $[0, 1]^T$ respectively. The eigenenergies in the right AM are $E_{e,\uparrow} = t_J[k_{ex}^2 a^2 + (k_{ey}a \pm \pi)^2] - \mu$ and $E_{h,\downarrow} = -t_J[(k_{hx}a - \pi)^2 + k_{hy}^2 a^2] + \mu$. Along k_x , we expand the Hamiltonian around $k_x = \pi/a$ and take the range of k_x to be $[0, 2\pi]$ for convenience. This does not change results. On the other hand, we take the range of k_y to be $[-\pi/a, \pi/a]$.

In the SC region, the dispersion is $E = \pm\sqrt{[\hbar^2(q_x^2 + q_y^2)/2m - \mu_s]^2 + \Delta^2}$. The eigenstates are Bogoliubov-de Gennes (BdG) quasiparticles, which have both the components: electron and hole. In the SC region, when the bias is within the superconducting energy gap, the BdG states are evanescent modes and are equally electron-like and hole-like. The eigenspinors are $[u_j, \Delta]^T$, where

$$\begin{aligned} u_j &= E + \frac{\hbar^2}{2m}(q_{xj}^2 + q_{yj}^2) - \mu, \quad \text{where } j = 1, 2, 3, 4, \\ q_{x1} &= \sqrt{\frac{2m}{\hbar^2}[\mu + \sqrt{E^2 - \Delta^2}] - q_y^2}, \\ q_{x2} &= -\sqrt{\frac{2m}{\hbar^2}[\mu + \sqrt{E^2 - \Delta^2}] - q_y^2}, \\ q_{x3} &= +\sqrt{\frac{2m}{\hbar^2}[\mu - \sqrt{E^2 - \Delta^2}] - q_y^2}, \\ q_{x4} &= -\sqrt{\frac{2m}{\hbar^2}[\mu - \sqrt{E^2 - \Delta^2}] - q_y^2}. \end{aligned} \quad (3)$$

An electron incident on the AM-SC interface from the left, results in four processes which can happen as said above. The wave function corresponding to this in different regions has the form $\psi e^{ik_{ey}y}$, where ψ is given by

$$\begin{aligned} \psi &= e^{ik_{exr}x} \begin{bmatrix} 1 \\ 0 \end{bmatrix} + r_{\uparrow_e} e^{i k_{exl}x} \begin{bmatrix} 1 \\ 0 \end{bmatrix} \\ &\quad + r_{\downarrow_h} e^{i k_{hx}x} \begin{bmatrix} 0 \\ 1 \end{bmatrix}, \quad \text{for } x < 0 \\ &= \sum_{j=1}^4 B_j e^{iq_{xj}x} \begin{bmatrix} u_j \\ \Delta \end{bmatrix}, \quad \text{for } 0 < x < L \\ &= t_{\uparrow_e} e^{ik'_{ex}x} \begin{bmatrix} 1 \\ 0 \end{bmatrix} + t_{\downarrow_h} e^{-ik'_{hx}x} \begin{bmatrix} 0 \\ 1 \end{bmatrix}, \quad \text{for } x > L \end{aligned} \quad (4)$$

where $r_{\uparrow_e}, r_{\downarrow_h}, t_{\uparrow_e}$ and t_{\downarrow_h} are the coefficients for the processes: ER, AR, ET and CAR respectively. Here, $k_{exr} = \pi/a + k_e \cos\theta$, and $k_{exl} = \pi/a - k_e \cos\theta$ denote the wave vector of right moving electron and left moving electron respectively, $k_{hx} = \sqrt{k_h^2 - (k_{ey} - \pi \text{sign}(\theta)/a)^2}$ is the wave vector of hole associated with Andreev reflected hole, $k'_{ex} = \sqrt{k_e^2 - (k_{ey} - \pi \text{sign}(\theta)/a)^2}$, $k'_{hx\downarrow} = \pi/a - \sqrt{(k_h^2 - k_{ey}^2)}$ are the wave vectors of electron and

hole which are associated with ET and CAR respectively, where $k_e a = \sqrt{(\mu + E)/t_J}$ and $k_h a = \sqrt{(\mu - E)/t_J}$. Due to the translational invariance along y direction, we have $q_y = k_{ey} = k_e \sin \theta$. Here, we choose the parameters so that k_{hx} and k'_{ex} are imaginary. This means that AR and ET are absent. k_{hx} (k'_{ex}) has a negative (positive) imaginary part.

Now, to determine the scattering coefficients, boundary conditions are needed. These can be determined by demanding conservation of probability current density along x -direction. The probability current densities along x direction on the left AM- $J_{L,AM}^P$, on the SC- J_{SC}^P , and on the right AM- $J_{R,AM}^P$ are given by

$$\begin{aligned} J_{L,AM}^P &= t_J a^2 [2\text{Im}(\psi^\dagger \tau_z \partial_x \psi) - \pi \psi^\dagger (\tau_z + \tau_0) \psi / a] / \hbar, \\ J_{SC}^P &= \hbar \text{Im}[\psi^\dagger \tau_z \partial_x \psi] / m, \\ J_{R,AM}^P &= t_J a^2 [2\text{Im}(\psi^\dagger \tau_z \partial_x \psi) - \pi \psi^\dagger (\tau_z - \tau_0) \psi / a] / \hbar \end{aligned} \quad (5)$$

The boundary conditions that conserve probability current density along x -direction are:

$$\begin{aligned} \psi(0^-) &= c\psi(0^+), \\ \psi(L^-) &= c\psi(L^+), \\ \left(\frac{\hbar^2}{2m a^2 t_J} \partial_x \psi - q_0 \psi\right)_{0^+} &= c \begin{pmatrix} \partial_x \psi_e - i \frac{\pi}{a} \psi_e \\ \partial_x \psi_h \end{pmatrix}_{0^-} \\ c \left(\frac{\hbar^2}{2m a^2 t_J} \partial_x \psi + q_0 \psi\right)_{L^-} &= \begin{pmatrix} \partial_x \psi_e \\ \partial_x \psi_h - i \frac{\pi}{a} \psi_h \end{pmatrix}_{L^+} \end{aligned} \quad (6)$$

where $\psi = [\psi_e, \psi_h]^T$. The parameter q_0 used in the

boundary conditions quantifies the strength of the delta-function barrier at the interface⁴⁵. The parameter c is real and dimensionless. Physically it corresponds to the strength of hopping from AM to SC in an equivalent lattice model¹⁶. We choose $c = 1$. Using these boundary conditions on the wave function having the form in eq. (4), the scattering coefficients can be determined. In subsection III D, we will demonstrate the probability current conservation.

Charge density is given by $\rho_c = e\psi^\dagger \tau_z \psi$. Charge density does not commute with the Hamiltonian in the SC region, though it commutes with the Hamiltonian's in the AMs. By using the continuity equation, we find charge current density on the left and the right AMs. The expressions for the charge current densities on the left and right AMs upon substituting the form of the wave function, are given by

$$\begin{aligned} I_{L,\uparrow e,\downarrow h} &= \frac{2et_J}{\hbar} [k_e \cos \theta (1 - |r_{\uparrow e}|^2)] \\ I_{R,\uparrow e,\downarrow h} &= \frac{2et_J}{\hbar} [(k'_{hx\downarrow} - \pi/a) |t_{\downarrow h}|^2] \end{aligned} \quad (7)$$

B. ($\downarrow e, \uparrow h$) sector

In this sector, the calculation of currents can be done in a way similar to that followed in the previous subsection. For completeness, below we mention the Hamiltonian, boundary conditions, the scattering eigenfunction and the charge current density. The Hamiltonian for this sector is given by $\sum_{\vec{k}} \Psi_{\vec{k}}^\dagger H_{\vec{k}} \Psi_{\vec{k}}$, where $\Psi_{\vec{k}} = [c_{\downarrow,k}, -c_{\uparrow,-k}]^T$ and

$$H_{\vec{k}} = \begin{cases} [t_J(k_x^2 a^2 + (k_y a \pm \pi)^2) - \mu] \frac{\tau_z + \tau_0}{2} + [t_J((k_x a \pm \pi)^2 + k_y^2 a^2) - \mu] \frac{\tau_z - \tau_0}{2}, & \text{for } x < 0, \\ \left[\frac{\hbar^2 (k_x^2 + k_y^2)}{2m} - \mu_s \right] \tau_z + \Delta \tau_x, & \text{for } 0 < x < L, \\ [t_J((k_x a \pm \pi)^2 + k_y^2 a^2) - \mu] \frac{\tau_z + \tau_0}{2} + [t_J(k_x^2 a^2 + (k_y a \pm \pi)^2) - \mu] \frac{\tau_z - \tau_0}{2}, & \text{for } x > L. \end{cases} \quad (8)$$

The wave function corresponding to an electron incident from the left AM onto the interface at energy E and angle of incidence θ has the form $\psi e^{ik_{ey}y}$, where ψ is

$$\begin{aligned} \psi &= e^{ik_{ex}x} \begin{bmatrix} 1 \\ 0 \end{bmatrix} + r_{\downarrow e} e^{-ik_{ex}x} \begin{bmatrix} 1 \\ 0 \end{bmatrix} + r_{\uparrow h} e^{ik_{hx}x} \begin{bmatrix} 0 \\ 1 \end{bmatrix}, \\ &\text{for } x < 0 \\ &= \sum_{j=1}^4 B_j e^{iq_{xj}x} \begin{bmatrix} u_j \\ \Delta \end{bmatrix}, \quad \text{for } 0 < x < L \\ &= t_{\downarrow e} e^{ik'_{ex}x} \begin{bmatrix} 1 \\ 0 \end{bmatrix} + t_{\uparrow h} e^{ik'_{hx\uparrow}x} \begin{bmatrix} 0 \\ 1 \end{bmatrix}, \quad \text{for } x > L \end{aligned} \quad (9)$$

Here, $k_{ex} = k_e \cos \theta$ denotes the wave vector of right moving electron. $k_{hx} = \pi/a + \sqrt{k_h^2 - k_{ey}^2}$ denotes the wave vector of hole in the region $x < 0$. $k_{ey} = \pi \text{sign}(\theta)/a - k_e \sin \theta$ whereas $k'_{ex} = \pi/a + \sqrt{k_e^2 - k_{ey}^2}$, $k'_{hx\uparrow} = -\sqrt{k_h^2 - (k_{ey} - \pi \text{sign}(\theta)/a)^2}$ stand for the wave vector of electron and hole in the right AM ($k_e a = \sqrt{(\mu + E)/t_J}$ and $k_h a = \sqrt{(\mu - E)/t_J}$). $\text{Im}(k_{hx}) < 0$

and $\text{Im}(k'_{ex}) > 0$. The boundary conditions are

$$\begin{aligned} \psi(0^-) &= \psi(0^+), \\ \left(\begin{array}{c} \partial_x \psi_e \\ \partial_x \psi_h - i \frac{\pi}{a} \psi_h \end{array} \right)_{0^-} &= \left(\begin{array}{c} \hbar^2 \\ 2 m a^2 t_J \end{array} \partial_x \psi - q_0 \psi \right)_{0^+} \\ \psi(L^-) &= \psi(L^+), \\ \left(\frac{\hbar^2}{2 m a^2 t_J} \partial_x \psi + q_0 \psi \right)_{L^-} &= \left(\begin{array}{c} \partial_x \psi_e - i \frac{\pi}{a} \psi_e \\ \partial_x \psi_h \end{array} \right)_{L^+}, \end{aligned} \quad (10)$$

where $\psi = [\psi_e, \psi_h]^T$

Charge current densities on the left and right AM are given by

$$\begin{aligned} I_{L,\downarrow e,\uparrow h} &= \frac{2 e t_J}{\hbar} [k_{ex} (1 - |r_{\downarrow e}|^2)] \\ I_{R,\downarrow e,\uparrow h} &= \frac{2 e t_J}{\hbar} [k'_{hx\uparrow} |t_{\uparrow h}|^2] \end{aligned} \quad (11)$$

C. Conductivity

The total current densities on the two AMs are $I_L = I_{L,\uparrow e,\downarrow h} + I_{L,\downarrow e,\uparrow h}$ and $I_R = I_{R,\uparrow e,\downarrow h} + I_{R,\downarrow e,\uparrow h}$. The differential conductivities on the two sides under a bias V from left AM are given by

$$\begin{aligned} G_{LL} &= \frac{e^2}{2\pi\hbar} k_e \left[\int_{-\pi/2}^{\pi/2} (1 - |r_{\uparrow e}|^2) \cos \theta d\theta \right. \\ &\quad \left. + \int_{-\pi/2}^{\pi/2} (1 - |r_{\downarrow e}|^2) \cos \theta d\theta \right], \\ G_{RL} &= \frac{e^2}{2\pi\hbar} \left[\int_{-\theta_c}^{\theta_c} (k'_{hx\downarrow} - \pi/a) |t_{\downarrow h}|^2 d\theta + \right. \\ &\quad \left. \int_{-\theta_c}^{\theta_c} k'_{hx\uparrow} |t_{\uparrow h}|^2 d\theta \right], \end{aligned} \quad (12)$$

where $\theta_c = \sin^{-1}[\min(k_h/k_e, 1)]$. Here, G_{LL} is called the local conductivity and G_{RL} the nonlocal conductivity. The local conductivity corresponds to the fraction of incident electrons from the left AM that get passed on to the SC and the right AM. Note that in this case, AR is completely suppressed. The nonlocal conductivity purely gets contribution from CAR (since ET does not contribute in this case) and is a measure of how good the CAR is.

D. Results and Analysis

To begin with, we shall examine the probability current conservation. Let us consider an up-spin electron incident from the left AM. By substituting the wave function [eq. (4)] into the expressions for the probability currents in eq. (5), the condition $J_{L,AM}^P = J_{R,AM}^P$

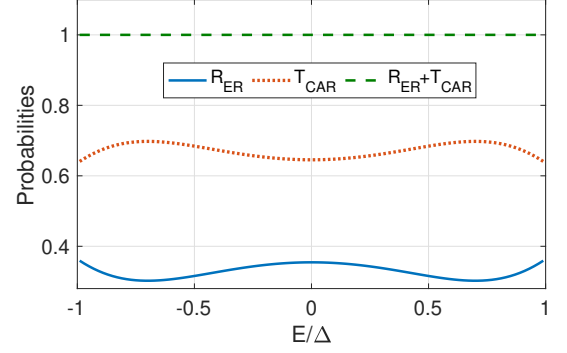


FIG. 3. Probabilities of ER (solid line) and CAR (dotted line), followed by their sum (dashed line) versus energy for \uparrow -spin electron incident from the left AM with $\theta = 0^+$, $q_0 = 0$, $L = 10.28a$, $m = \hbar^2/(a^2 t_J)$, $\mu = 0.2t_J$, $\Delta = 0.1t_J$ and $\mu_s = 2t_J$ are shown. For this case, the probabilities of AR and ET are zero. The plot exhibits probability current conservation.

implies that $1 = R_{ER} + T_{CAR}$, where $R_{ER} = |r_{\uparrow e}|^2$ and $T_{CAR} = |t_{\downarrow h}|^2(\pi/a - k'_{hx\downarrow})/k_e \cos \theta$. In Fig. 3, we plot the probabilities for ER and CAR: R_{ER} and T_{CAR} , followed by their sum versus energy E , choosing the parameters: $q_0 = 0$, $L = 10.28 a$, $m = \hbar^2/(a^2 t_J)$, $\mu = 0.2t_J$, $\Delta = 0.1t_J$ and $\mu_s = 2t_J$, $L = 10.28a$, and $\theta \rightarrow 0^+$.

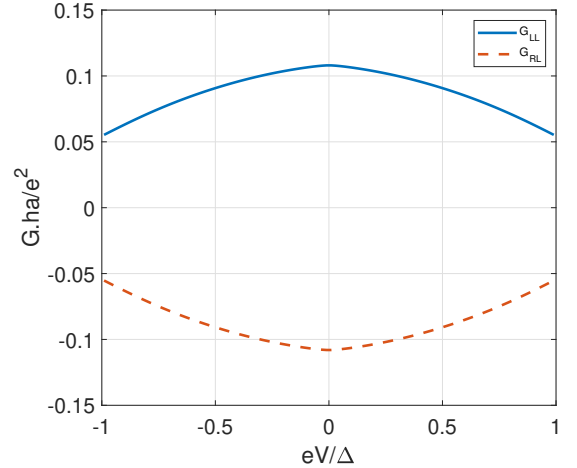


FIG. 4. Local conductivity (blue line) and non-local conductivity (red dashed line) versus bias for $q_0 = 0$, $L = 10.28a$, $m = \hbar^2/(a^2 t_J)$, $\mu = 0.2t_J$, $\Delta = 0.1t_J$ and $\mu_s = 2t_J$ are shown.

The local and nonlocal conductivities are numerically calculated following the procedure sketched in the previous subsections and plotted versus bias in Fig. 4 for the same set of parameters as earlier, except that θ is no more a parameter now. L is chosen to be $10.28a$ since CAR is enhanced for this choice of the length as can be seen in Fig. 5. We find that the local and non-local conductivity are exactly equal in magnitude and opposite in sign. This is because, there are only two processes that occur - CAR

and ER. And from probability current conservation, the probability currents are equal on the left and the right AM. But, the charge current due to ER is e times the probability current, whereas the charge current due to CAR is $-e$ times the probability current. This makes the charge currents on the two sides equal in magnitude and opposite in sign. The non-local conductivity shows a negative peak at zero energy. This is because for $E = 0$, k_e becomes exactly equal to k_h i.e., k_{ey} for all the incident electrons having momentum k_e , matches with k_{hy} for all the holes in the other AM having momentum k_h . So the conversion of electron to hole is maximum, giving rise to maximum CAR. But when energy $E \neq 0$, there is a mismatch in the transverse momentum values for \uparrow_e and \downarrow_h resulting in lower conductivity. The non-local conductivity here is predominantly due to the incident up-spin electrons. The contribution to conductivities from the incident down spin electrons is 10^{-9} times the contribution from incident up spin electrons. The reason behind this is that for down-spin electron incidence k_{ey} value is very large (near π) in comparison with k_{ey} value for up-spin electron incidence (near $k_{ey} = 0$). This results in a much smaller decay length for the evanescent modes in the SC region for the incident down spin electrons compared to that for the incident up spin electrons.

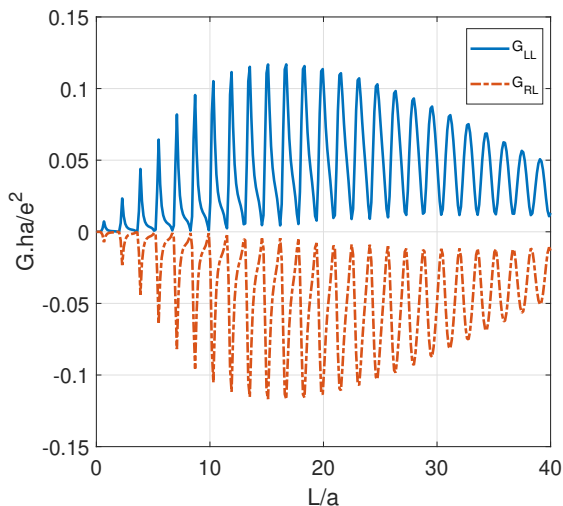


FIG. 5. Local (solid blue line) and non-local (dash-dotted red line) conductivity versus the length of SC region are shown for $q_0 = 0$, $eV = 0$, $m = \hbar^2/(a^2t_J)$, $\mu = 0.2t_J$, $\Delta = 0.1t_J$ and $\mu_s = 2t_J$.

Now, keeping all the parameters the same and fixing the bias to be at zero, we plot the conductivities versus length of the SC region in Fig. 5. The conductivities show oscillations due to Fabry-Pérot interference⁴⁶⁻⁴⁹ in the superconducting region. Within the SC gap, the wave numbers in the SC region are not purely real. The real part of the wave numbers is responsible for the Fabry-Pérot interference. The Fabry-Pérot interference condition is $\Delta L = \pi/k$, where ΔL is the separation between

the consecutive peaks and k is the real part of the wave number of the interfering mode in the SC. Here, we take the k for the normal incidence, since the dominant contribution to the nonlocal transport is due to the electrons incident normal to the interface. The value of ΔL calculated from this condition is $1.5695a$ in comparison to $1.6053a$ that is observed in the results in Fig. 5. Further, the peak value of the magnitude of non-local conductivity first increases with length, reaches a maximum value up to the order of 10^{-1} for superconducting length nearly equal to $15a$ and then gradually decreases. The global peak in the magnitude of nonlocal conductivity is due to maximum CAR which happens when the length of the SC is approximately inverse of the imaginary part of the wave number in the SC region, which is $20a$. This can be understood in the following way. Electron to hole conversion in SC is large within the SC gap. For small lengths of the SC, the electron to hole conversion is small. At small lengths, the electron to hole conversion probability increases with the length of the SC. But the wave function in the SC decays exponentially with the increase in the length of the SC and hence, for very large lengths of the SC, the converted hole does not reach the other AM. When the length of the SC is inverse of the imaginary part of the wave number, the electron to hole conversion is large and the wave function in the SC is optimum at the right SC-AM interface for the hole to exit into the right AM. The nonlocal conductivity is always negative for AMs in the strong phase chosen with appropriate crystallographic orientation, signalling dominant CAR with zero contribution from ET. We numerically find that the contribution to the current from ET is zero, which can be understood by looking at Fig. 2. Due to mismatch of k_y for the electron states on the two AMs, k_x on the right AM for \uparrow -spin electron is complex and hence the \uparrow -spin electron does not carry any current in the right AM. This is in contrast to other schemes of enhancement of CAR, wherein the contribution to nonlocal conductivity from ET is typically nonzero^{20,27,28,33}. It may be noted here that there exist proposals in literature, where 100% CAR can be achieved in principle³⁰⁻³².

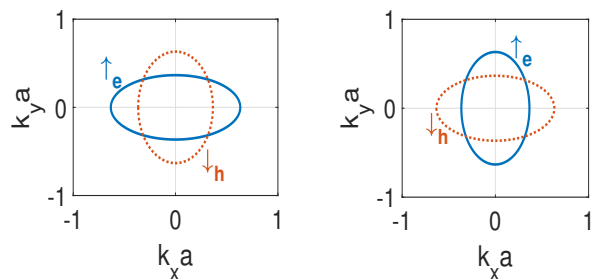


FIG. 6. Fermi surfaces of AMs on the left and the right in weak phase, blue solid line showing \uparrow_e and red dotted line shows \downarrow_h for $t_J = 0.5t_0$ and $\mu = 0.2t_0$

IV. ALTERMAGNETS IN WEAK PHASE

In this section, we choose the AMs to be in the weak phase by choosing $t_0 > t_J \geq 0$. Unlike in the strong phase, the band bottoms for both the spins are located at $k_x = k_y = 0$. But the Fermi surfaces do not overlap, rather they intersect each other due to their anisotropic behavior. As a result, for a given spin, all the k_y values for the electrons of AMs on either sides of the SC do not match. However, the k_y values for electrons of spin

σ on one side match with k_y values for holes of spin $\bar{\sigma}$ to a much larger extent. This can be seen from Fig. 6. Therefore, CAR is favored over ET on an average.

A. $(\uparrow_e, \downarrow_h)$ sector

In this sector, the Hamiltonian can be written similar to $(\uparrow_e, \downarrow_h)$ case in strong phase. The difference is that now the dispersion is expanded around $k_x = 0, k_y = 0$ as the band bottom lies there. The Hamiltonian is:

$$H_{\vec{k}} = \begin{cases} [(t_0 - t_J) k_x^2 a^2 + (t_0 + t_J) k_y^2 a^2 - \mu] \frac{\tau_x + \tau_0}{2} + [(t_0 + t_J) k_x^2 a^2 + (t_0 - t_J) k_y^2 a^2 - \mu] \frac{\tau_x - \tau_0}{2}, & \text{for } x < 0 \\ \left[\frac{\hbar^2 (k_x^2 + k_y^2)}{2m} - \mu_s \right] \tau_z + \Delta \tau_x, & \text{for } 0 < x < L \\ [(t_0 + t_J) k_x^2 a^2 + (t_0 - t_J) k_y^2 a^2 - \mu] \frac{\tau_x + \tau_0}{2} + [(t_0 - t_J) k_x^2 a^2 + (t_0 + t_J) k_y^2 a^2 - \mu] \frac{\tau_x - \tau_0}{2}, & \text{for } x > L \end{cases} \quad (13)$$

In Fig. 6, the Fermi surfaces for AMs on the two sides are shown. The wave function corresponding to the Hamiltonian in different regions possesses the form $\psi e^{ik_{ey}y}$, where ψ is given by

$$\begin{aligned} \psi &= e^{ik_{ex\uparrow}x} \begin{bmatrix} 1 \\ 0 \end{bmatrix} + r_{\uparrow_e} e^{-ik_{ex\uparrow}x} \begin{bmatrix} 1 \\ 0 \end{bmatrix} + r_{\downarrow_h} e^{ik_{hx\downarrow}x} \begin{bmatrix} 0 \\ 1 \end{bmatrix}, \\ &\quad \text{for } x < 0, \\ &= \sum_{j=1}^4 B_j e^{iq_{xj}x} \begin{bmatrix} u_j \\ \Delta \end{bmatrix}, \quad \text{for } 0 < x < L, \\ &= t_{\uparrow_e} e^{ik'_{ex\uparrow}x} \begin{bmatrix} 1 \\ 0 \end{bmatrix} + t_{\downarrow_h} e^{ik'_{hx\downarrow}x} \begin{bmatrix} 0 \\ 1 \end{bmatrix}, \quad \text{for } x > L, \end{aligned} \quad (14)$$

and $r_{\uparrow_e}, r_{\downarrow_h}, t_{\uparrow_e}$ and t_{\downarrow_h} are the scattering coefficients for ER, AR, ET and CAR respectively. Here, $k_{ex\uparrow}a = \sqrt{(E + \mu)/(t_0 - t_J)} \cos \theta$ is the wave vector associated with right moving electron, $k_{ey}a = \sqrt{(E + \mu)/(t_0 + t_J)} \sin \theta$ is the component of wave vector of electron along y -direction. $k_{hx\downarrow}a = \sqrt{[(\mu - E) - (t_0 - t_J) k_{ey}^2 a^2]/(t_0 + t_J)}$ is the wave vector associated with reflected hole in left AM whereas $k'_{ex\uparrow}a = \sqrt{[(\mu + E) - (t_0 - t_J) k_{ey}^2 a^2]/(t_0 + t_J)}$ and $k'_{hx\downarrow}a = -\sqrt{[(\mu - E) - (t_0 + t_J) k_{ey}^2 a^2]/(t_0 - t_J)}$ stand for the wave vectors for the transmitted electron and transmitted hole respectively. Whenever any of these wave numbers turn out to be complex, the square root is taken so that the wave decays to zero at $x \rightarrow \pm\infty$.

The probability current density along x direction on: the left AM- $J_{L,AM}^P$, central SC- J_{SC}^P and the right AM- $J_{R,AM}^P$ are given by

$$\begin{aligned} J_{L,AM}^P &= \frac{(t_0 - t_J)a^2 [\text{Im}(\psi^\dagger (\tau_z + \tau_0) \partial_x \psi)] - (t_0 + t_J)a^2 [\text{Im}(\psi^\dagger (\tau_z - \tau_0) \partial_x \psi)]}{\hbar} \\ J_{SC}^P &= \frac{\hbar \text{Im}[\psi^\dagger \tau_z \partial_x \psi]}{m} \\ J_{R,AM}^P &= \frac{(t_0 + t_J)a^2 [\text{Im}(\psi^\dagger (\tau_z + \tau_0) \partial_x \psi)] - (t_0 - t_J)a^2 [\text{Im}(\psi^\dagger (\tau_z - \tau_0) \partial_x \psi)]}{\hbar} \end{aligned} \quad (15)$$

From probability current conservation on the two sides, we can find the boundary conditions which will ultimately help us in determining the scattering coefficients.

We choose the following boundary conditions:

$$\begin{aligned} \psi(0^-) &= \psi(0^+), \\ \partial_x \psi|_{0^-} &= \left(\frac{\hbar^2}{2ma^2(t_0 - t_J)} \partial_x \psi_e - q_0 \psi_e \right)_{0^+} \\ &\quad - \left(\frac{\hbar^2}{2ma^2(t_0 + t_J)} \partial_x \psi_h - q_0 \psi_h \right)_{0^+} \\ \psi(L^+) &= \psi(L^-), \\ \partial_x \psi|_{L^+} &= \left(\frac{\hbar^2}{2ma^2(t_0 + t_J)} \partial_x \psi_e + q_0 \psi_e \right)_{L^-} \\ &\quad - \left(\frac{\hbar^2}{2ma^2(t_0 - t_J)} \partial_x \psi_h + q_0 \psi_h \right)_{L^-} \end{aligned} \quad (16)$$

Charge current density in the left and the right AM are

$$\begin{aligned}
I_{L,\uparrow e,\downarrow h} &= \frac{2e}{\hbar} [(t_0 - t_J)k_e \cos \theta (1 - |r_{\uparrow e}|^2) \\
&\quad + (t_0 + t_J)\text{Re}(k_{hx\downarrow})|r_{\downarrow h}|^2] \\
I_{R,\uparrow e,\downarrow h} &= \frac{2e}{\hbar} [(t_0 + t_J)\text{Re}(k'_{ex\uparrow})|t_{\uparrow e}|^2 \\
&\quad + (t_0 - t_J)\text{Re}(k'_{hx\downarrow})|t_{\downarrow h}|^2]
\end{aligned} \tag{17}$$

B. (\downarrow_e, \uparrow_h) sector

We use a method similar to that in the previous subsection to find the current density in this sector. So we start with the Hamiltonian:

$$H_{\vec{k}} = \begin{cases} [(t_0 + t_J) k_x^2 a^2 + (t_0 - t_J) k_y^2 a^2 - \mu] \frac{\tau_x + \tau_0}{2} + [(t_0 - t_J) k_x^2 a^2 + (t_0 + t_J) k_y^2 a^2 - \mu] \frac{\tau_x - \tau_0}{2}, & \text{for } x < 0 \\ \left[\frac{\hbar^2 (k_x^2 + k_y^2)}{2m} - \mu_s \right] \tau_z + \Delta \tau_x, & \text{for } 0 < x < L \\ [(t_0 - t_J) k_x^2 a^2 + (t_0 + t_J) k_y^2 a^2 - \mu] \frac{\tau_x + \tau_0}{2} + [(t_0 + t_J) k_x^2 a^2 + (t_0 - t_J) k_y^2 a^2 - \mu] \frac{\tau_x - \tau_0}{2}, & \text{for } x > L \end{cases} \tag{18}$$

The wave function for the system has the form $\psi e^{ik_{ey}y}$ where

$$\begin{aligned}
\psi &= e^{ik_{ex\downarrow}x} \begin{bmatrix} 1 \\ 0 \end{bmatrix} + r_{\downarrow e} e^{-ik_{ex\downarrow}x} \begin{bmatrix} 1 \\ 0 \end{bmatrix} + r_{\uparrow h} e^{ik_{hx\uparrow}x} \begin{bmatrix} 0 \\ 1 \end{bmatrix}, \\
&\quad \text{for } x < 0 \\
&= \sum_{j=1}^4 B_j e^{iq_{xj}x} \begin{bmatrix} u_j \\ \Delta \end{bmatrix}, \quad \text{for } 0 < x < L \\
&= t_{\downarrow e} e^{ik'_{ex\downarrow}x} \begin{bmatrix} 0 \\ 1 \end{bmatrix} + t_{\uparrow h} e^{ik'_{hx\uparrow}x} \begin{bmatrix} 1 \\ 0 \end{bmatrix}, \quad \text{for } x > L, \tag{19}
\end{aligned}$$

$$\begin{aligned}
&\text{and } k_{ex\downarrow}a = \sqrt{(E + \mu)/(t_0 + t_J)} \cos \theta, \\
&k_{ey}a = \sqrt{(E + \mu)/(t_0 - t_J)} \sin \theta, \\
&k_{hx\uparrow}a = \sqrt{[(\mu - E) - (t_0 + t_J) k_{ey}^2 a^2]/(t_0 - t_J)}, \\
&k'_{ex\downarrow}a = \sqrt{[(E + \mu) - (t_0 + t_J) k_{ey}^2 a^2]/(t_0 - t_J)}, \\
&k'_{hx\uparrow}a = -\sqrt{[(\mu - E) - (t_0 - t_J) k_{ey}^2 a^2]/(t_0 + t_J)}.
\end{aligned}$$

All the above terms have the same meaning as mentioned in the previous subsection. The boundary conditions for

given by the following expressions:

this sector are given by

$$\begin{aligned}
\psi(0^-) &= \psi(0^+), \\
\partial_x \psi|_{0^-} &= \left(\frac{\hbar^2}{2ma^2(t_0 + t_J)} \partial_x \psi_e - q_0 \psi_e \right) \\
&\quad \left(\frac{\hbar^2}{2ma^2(t_0 - t_J)} \partial_x \psi_h - q_0 \psi_h \right)_{0^+} \\
\psi(L^+) &= \psi(L^-), \\
\partial_x \psi|_{L^+} &= \left(\frac{\hbar^2}{2ma^2(t_0 - t_J)} \partial_x \psi_e + q_0 \psi_e \right) \\
&\quad \left(\frac{\hbar^2}{2ma^2(t_0 + t_J)} \partial_x \psi_h + q_0 \psi_h \right)_{L^-}
\end{aligned} \tag{20}$$

Charge current density in the left and right AM are given by the following expressions:

$$\begin{aligned}
I_{L,\downarrow e,\uparrow h} &= \frac{2e}{\hbar} [(t_0 + t_J)k_e \cos \theta (1 - |r_{\downarrow e}|^2) \\
&\quad + (t_0 - t_J)\text{Re}(k_{hx\uparrow})|r_{\uparrow h}|^2] \\
I_{R,\downarrow e,\uparrow h} &= \frac{2e}{\hbar} [(t_0 - t_J)\text{Re}(k'_{ex\downarrow})|t_{\downarrow e}|^2 \\
&\quad + (t_0 + t_J)\text{Re}(k'_{hx\uparrow})|t_{\uparrow h}|^2]
\end{aligned} \tag{21}$$

C. Conductivity

The total current densities on the two AMs are $I_L = I_{L,\uparrow e,\downarrow h} + I_{L,\downarrow e,\uparrow h}$ and $I_R = I_{R,\uparrow e,\downarrow h} + I_{R,\downarrow e,\uparrow h}$. Unlike in the case of AMs in the strong phase, here the local conductivity draws contributions from ER and AR. Similarly, the nonlocal conductivity gets contributions from ET and CAR. Negative value of nonlocal conductivity means that CAR overpowers ET. The differential conductivities on the two sides under a bias V from left AM are given by

$$G_{LL} = \frac{e^2}{2\pi h} \left[\sqrt{\frac{t_0 - t_J}{t_0 + t_J}} \int_{-\pi/2}^{\pi/2} k_{ex\uparrow} (1 - |r_{\uparrow e}|^2) d\theta + \sqrt{\frac{t_0 + t_J}{t_0 - t_J}} \int_{-\theta_{h\downarrow}}^{\theta_{h\downarrow}} k_{hx\downarrow} (|r_{\downarrow h}|^2) d\theta \right. \\ \left. + \sqrt{\frac{t_0 + t_J}{t_0 - t_J}} \int_{-\pi/2}^{\pi/2} k_{ex\downarrow} (1 - |r_{\downarrow e}|^2) d\theta + \sqrt{\frac{t_0 - t_J}{t_0 + t_J}} \int_{-\theta_{h\uparrow}}^{\theta_{h\uparrow}} k_{hx\uparrow} (|r_{\uparrow h}|^2) d\theta \right], \quad (22)$$

$$\text{where } \theta_{h\downarrow} = \sin^{-1} \left[\min \left[\frac{(\mu - E)(t_0 + t_J)}{(\mu + E)(t_0 - t_J)}, 1 \right] \right], \quad \theta_{h\uparrow} = \sin^{-1} \left[\min \left[\frac{(\mu - E)(t_0 - t_J)}{(\mu + E)(t_0 + t_J)}, 1 \right] \right],$$

$$G_{RL} = \frac{e^2}{2\pi h} \left[\sqrt{\frac{t_0 + t_J}{t_0 - t_J}} \int_{-\pi/2}^{\pi/2} k'_{ex\uparrow} (|t_{\uparrow e}|^2) d\theta - \sqrt{\frac{t_0 - t_J}{t_0 + t_J}} \int_{-\theta_h}^{\theta_h} k'_{hx\downarrow} (|t_{\downarrow h}|^2) d\theta \right. \\ \left. + \sqrt{\frac{t_0 - t_J}{t_0 + t_J}} \int_{-\theta_e}^{\theta_e} k'_{ex\downarrow} (|t_{\downarrow e}|^2) d\theta - \sqrt{\frac{t_0 + t_J}{t_0 - t_J}} \int_{-\theta_h}^{\theta_h} k'_{hx\uparrow} (|t_{\uparrow h}|^2) d\theta \right], \quad (23)$$

$$\text{where } \theta_e = \sin^{-1} \left[\sqrt{(t_0 - t_J)/(t_0 + t_J)} \right], \quad \theta_h = \sin^{-1} \left[\min \{ (\mu - E)/(\mu + E), 1 \} \right].$$

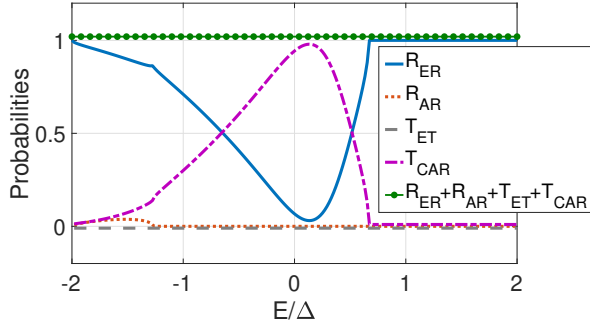


FIG. 7. Probabilities of ER (solid line), AR (dotted line), ET (dashed line), CAR (dot-dash line) and their sum (flat points line) versus energy E for a \downarrow -spin electron incident from the left AM with $\theta = \pi/4$, $q_0 = 0$, $L = 7a$, $t_J = 0.8t_0$ $m = \hbar^2/(a^2t_0)$, $\mu = 0.2t_0$, $\Delta = 0.1t_0$ and $\mu_s = 2t_0$ are shown.

D. Results and Analysis

We begin this subsection by demonstrating probability current conservation. For the weak phase, all four processes - ER, AR, ET and CAR contribute to probability current. Let us consider a down spin electron incident from the left AM. It can be shown that the probabilities of ER, AR, ET and CAR are respectively given by

$$R_{ER} = |r_{\downarrow e}|^2, \\ R_{AR} = \frac{(t_0 - t_J) |\text{Re}(k_{h\uparrow})| |r_{\uparrow h}|^2}{(t_0 + t_J) k_e \cos \theta}, \\ T_{ET} = \frac{(t_0 - t_J) \text{Re}(k'_{ex\downarrow}) |t_{e\downarrow}|^2}{(t_0 + t_J) k_e \cos \theta}, \\ T_{CAR} = \frac{|\text{Re}(k'_{hx\uparrow})| |t_{\uparrow h}|^2}{k_e \cos \theta}. \quad (24)$$

In Fig. 7, we plot these probabilities and their sum versus energy for $\theta = \pi/4$, $q_0 = 0$, $L = 7a$, $t_J = 0.8t_0$ $m =$

$\hbar^2/(a^2t_0)$, $\mu = 0.2t_0$, $\Delta = 0.1t_0$ and $\mu_s = 2t_0$. It can be seen that the probabilities for the four processes add up to 1. Though for the angle of incidence $\theta = \pi/4$, the down-spin electron exhibits almost perfect CAR near zero energy for this choice of parameters.

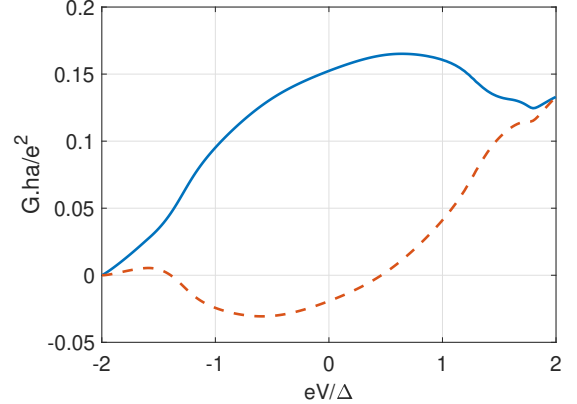


FIG. 8. Local conductivity (blue line) and non-local conductivity (red dashed line) versus bias for $q_0 = 0$, $L = 7a$, $t_J = 0.8t_0$ $m = \hbar^2/(a^2t_0)$, $\mu = 0.2t_0$, $\Delta = 0.1t_0$ and $\mu_s = 2t_0$ are shown.

In Fig. 8, we plot the two conductivities versus bias and find that CAR dominates over ET for a certain range of bias within the SC gap. Because, within the superconducting gap, the electron to hole conversion has higher probability. In Fig.9, the variation of non-local conductivity with length for different values of t_J is shown. $t_J = 0$ corresponds to the absence of altermagnetic phase, and the leads behave as normal metal leads. We notice that when $t_J \neq 0$ the non-local conductivity is higher in magnitude as compared to when $t_J = 0$. Thus, we find that AM helps to enhance CAR in comparison to a normal metal. The larger the value of t_J within the range $0 < t_J < t_0$, the larger is the non-local conductivity in magnitude. The non-local conductivity plot shows

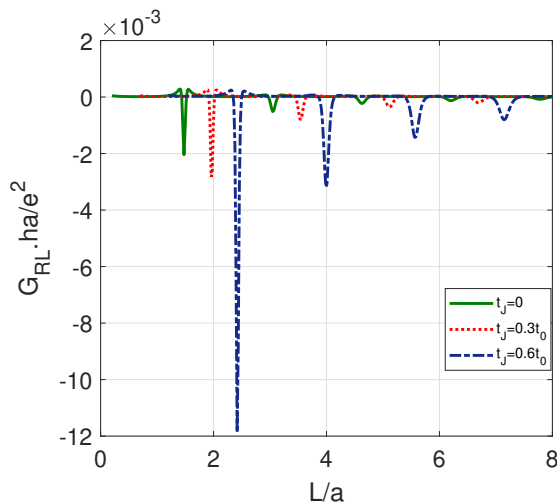


FIG. 9. Non-local conductivity versus length of SC for $t_J = 0$ (green solid line), $t_J = 0.3t_0$ (red dotted-line), $t_J = 0.6t_0$ (blue dash-dot line), $E = 0$, $q_0 = 10t_0$, $m = \hbar^2/(a^2t_0)$, $\mu = 0.2t_0$, $\Delta = 0.1t_0$, $\mu_s = 2t_0$. Red dotted and blue dash-dot curves are shifted by 0.5 and 1.0 units along x -axis respectively for clarity.

a negative peak for some definite values of length, and this peak is periodic in nature. The reason behind this is that the wave gets multiply reflected back-and-forth within the SC region and picks up a phase of $2\text{Re}(q_x)L$ in one round of back-and-forth reflection, where q_x is the wave number in the SC region. According to the Fabry-Pérot interference condition, when this phase difference is integral multiple of 2π , we get constructive interference resulting in peaks. The separation between two consecutive negative peaks can be calculated by $\Delta L = \pi/\text{Re}(q_x)$. The value of ΔL calculated from this formula is $1.57a$ and the value observed in Fig. 9 is $\sim 1.58a$.

V. EXPERIMENTAL RELEVANCE

Let us see how the parameters t_0 and t_J used in the model are connected to real materials, taking the example of RuO_2 - a well established AM. In RuO_2 , the bandwidth and the spin splitting are of the same order of

magnitude $\sim 1eV^{10,50}$. However, the SC gap in conventional SCs like NbSe_2 is of the order of a few meV making the ratio of $\Delta/t_0 \sim 10^{-3}$. The nonlocal conductivity is not negative for such a choice of parameters. To get negative nonlocal conductivity, Δ/t_0 needs to be of the order of 0.1 maintaining $t_J \sim t_0$. This can be achieved by choosing Mn_5Si_3 for AM which has a spin splitting of 150 meV⁴¹. For this material, the estimated values of $t_J \simeq 2t_0 \sim 150\text{meV}$. Some of the iron based SCs have a larger SC gap^{51–55}. In particular, the material $(\text{Tl}_{0.58}\text{Rb}_{0.42})\text{Fe}_{1.72}\text{Se}_2$ has an SC gap of 15meV⁵⁵. The choice of such iron based SC along with the AM Mn_5Si_3 will give us $\Delta/t_0 \sim 0.1$ along with $t_J \gtrsim t_0$ which is suited to test the predictions of our work.

VI. CONCLUSION

We propose to employ the newly discovered AMs to enhance and detect crossed Andreev reflection across an s-wave SC. When the two AMs are rotated by 90° with respect to each other, CAR can be enhanced significantly. We calculated the local and nonlocal conductivities for AM-SC-AM junctions. We find that when the AMs are in the strong phase, the nonlocal transport can be completely dominated by CAR with zero contribution from ET. On the other hand, when the AMs are in the weak phase, both ET and CAR contribute to the nonlocal conductivity. But, for certain choice of parameters, we can get larger contribution from CAR than from ET. The nonlocal conductivity shows extrema for certain values of the length of the SC which is rooted in Fabry-Pérot type interference. With a careful choice of the length of the SC, the system can be tuned to enhance CAR. Our results will be useful in development of superconducting devices based on the phenomenon of CAR.

ACKNOWLEDGMENTS

We thank Dhavala Suri for illuminating discussions. SD and AS thank SERB Core Research grant (CRG/2022/004311) for financial support. AS thanks the funding from University of Hyderabad Institute of Eminence PDF.

* abhiraams@uohyd.ac.in

¹ S. A. Wolf, D. D. Awschalom, R. A. Buhrman, J. M. Daughton, S. von Molnár, M. L. Roukes, A. Y. Chtchelkanova, and D. M. Treger, “Spintronics: A spin-based electronics vision for the future,” *Science* **294**, 1488–1495 (2001).

² C. Chappert, A. Fert, and F. Van Dau, “The emergence of spin electronics in data storage,” *Nat. Mater.* **6**, 813–823 (2007).

³ V. Baltz, A. Manchon, M. Tsoi, T. Moriyama, T. Ono, and Y. Tserkovnyak, “Antiferromagnetic spintronics,” *Rev. Mod. Phys.* **90**, 015005 (2018).

⁴ S. Fukami, V. O. Lorenz, and O. Gomonay, “Antiferromagnetic spintronics,” *J. Appl. Phys.* **128**, 070401 (2020).

⁵ A. Hoffmann and W. Zhang, “Antiferromagnets for spintronics,” *J. Magn. Magn. Mater.* **553**, 169216 (2022).

⁶ J. Sinova, D. Culcer, Q. Niu, N. A. Sinitsyn, T. Jungwirth, and A. H. MacDonald, “Universal intrinsic spin Hall effect,” *Phys. Rev. Lett.* **92**, 126603 (2004).

- ⁷ B. K. Sahoo and A. Soori, “Transverse currents in spin transistors,” *J. Phys.: Condens. Matter* **35**, 365302 (2023).
- ⁸ L. Šmejkal, A. B. Hellenes, R. González-Hernández, J. Sinova, and T. Jungwirth, “Giant and tunneling magnetoresistance in unconventional collinear antiferromagnets with nonrelativistic spin-momentum coupling,” *Phys. Rev. X* **12**, 011028 (2022).
- ⁹ L. Šmejkal, J. Sinova, and T. Jungwirth, “Beyond conventional ferromagnetism and antiferromagnetism: A phase with nonrelativistic spin and crystal rotation symmetry,” *Phys. Rev. X* **12**, 031042 (2022).
- ¹⁰ L. Šmejkal, J. Sinova, and T. Jungwirth, “Emerging research landscape of altermagnetism,” *Phys. Rev. X* **12**, 040501 (2022).
- ¹¹ R. M. Fernandes, V. S. de Carvalho, T. Birol, and R. G. Pereira, “Topological transition from nodal to nodeless Zeeman splitting in altermagnets,” *Phys. Rev. B* **109**, 024404 (2024).
- ¹² C. Sun, A. Brataas, and J. Linder, “Andreev reflection in altermagnets,” *Phys. Rev. B* **108**, 054511 (2023).
- ¹³ X. Zhou, W. Feng, E.-W. Zhang, L. Šmejkal, J. Sinova, Y. Mokrousov, and Y. Yao, “Crystal thermal transport in altermagnetic RuO_2 ,” *Phys. Rev. Lett.* **132**, 056701 (2024).
- ¹⁴ H. Yan, X. Zhou, P. Qin, and Z. Liu, “Review on spin-split antiferromagnetic spintronics,” *App. Phys. Lett.* **124**, 030503 (2024).
- ¹⁵ H. Reichlova, D. Kriegner, A. Mook, M. Althammer, and A. Thomas, “Role of topology in compensated magnetic systems,” *APL Mater.* **12**, 010902 (2024).
- ¹⁶ S. Das, D. Suri, and A. Soori, “Transport across junctions of altermagnets with normal metals and ferromagnets,” *J. Phys.: Condens. Matter* **35**, 435302 (2023).
- ¹⁷ S. Hayami, Y. Yanagi, and H. Kusunose, “Momentum-dependent spin splitting by collinear antiferromagnetic ordering,” *J. Phys. Soc. Jpn* **88**, 123702 (2019).
- ¹⁸ S. Hayami, Y. Yanagi, and H. Kusunose, “Bottom-up design of spin-split and reshaped electronic band structures in antiferromagnets without spin-orbit coupling: Procedure on the basis of augmented multipoles,” *Phys. Rev. B* **102**, 144441 (2020).
- ¹⁹ I. Mazin and L. Šmejkal R. Gonzalez-Hernandez, “Induced monolayer altermagnetism in $\text{MnP}(\text{S,Se})_3$ and FeSe ,” arXiv:2309.02355 (2023).
- ²⁰ D. Beckmann, H. B. Weber, and H. v. Löhneysen, “Evidence for crossed Andreev reflection in superconductor-ferromagnet hybrid structures,” *Phys. Rev. Lett.* **93**, 197003 (2004).
- ²¹ P. Recher, E. V. Sukhorukov, and D. Loss, “Andreev tunneling, coulomb blockade, and resonant transport of non-local spin-entangled electrons,” *Phys. Rev. B* **63**, 165314 (2001).
- ²² A. Das, Y. Ronen, M. Heiblum, D. Mahalu, A. V. Kretinin, and H. Shtrikman, “High-efficiency cooper pair splitting demonstrated by two-particle conductance resonance and positive noise cross-correlation,” *Nature Communications* **3**, 1165 (2012).
- ²³ J. Schindele, A. Baumgartner, and C. Schönenberger, “Near-unity cooper pair splitting efficiency,” *Phys. Rev. Lett.* **109**, 157002 (2012).
- ²⁴ N. M. Chtchelkatchev, “Superconducting spin filter,” *JETP Lett.* **78**, 230 (2003).
- ²⁵ R. Mélin and D. Feinberg, “Sign of the crossed conductances at a ferromagnet/superconductor/ferromagnet double interface,” *Phys. Rev. B* **70**, 174509 (2004).
- ²⁶ I. A. Sadovskyy, G. B. Lesovik, and V. M. Vinokur, “Unitary limit in crossed Andreev transport,” *New J. Phys.* **17**, 103016 (2015).
- ²⁷ A. Soori and S. Mukerjee, “Enhancement of crossed Andreev reflection in a superconducting ladder connected to normal metal leads,” *Phys. Rev. B* **95**, 104517 (2017).
- ²⁸ R. Nehra, D. S. Bhakuni, A. Sharma, and A. Soori, “Enhancement of crossed Andreev reflection in a Kitaev ladder connected to normal metal leads,” *J. Phys.: Condens. Matter* **31**, 345304 (2019).
- ²⁹ A. Soori, “Tunable crossed Andreev reflection in a heterostructure consisting of ferromagnets, normal metal and superconductors,” *Solid State Commun.* **348-349**, 114721 (2022).
- ³⁰ S.-B. Zhang and B. Trauzettel, “Perfect crossed Andreev reflection in Dirac hybrid junctions in the quantum hall regime,” *Phys. Rev. Lett.* **122**, 257701 (2019).
- ³¹ M. F. Jakobsen, A. Brataas, and A. Qaiumzadeh, “Electrically controlled crossed Andreev reflection in two-dimensional antiferromagnets,” *Phys. Rev. Lett.* **127**, 017701 (2021).
- ³² S.-C. Zhao, L. Gao, Q. Cheng, and Q.-F. Sun, “Perfect crossed andreev reflection in the proximitized graphene/superconductor/proximitized graphene junctions,” *Phys. Rev. B* **108**, 134511 (2023).
- ³³ S. Russo, M. Kroug, T. M. Klapwijk, and A. F. Morpurgo, “Experimental observation of bias-dependent nonlocal Andreev reflection,” *Phys. Rev. Lett.* **95**, 027002 (2005).
- ³⁴ S. O. Valenzuela and M. Tinkham, “Direct electronic measurement of the spin hall effect,” *Nature* **442**, 176–179 (2006).
- ³⁵ J. S. Moodera, L. R. Kinder, T. M. Wong, and R. Meservey, “Large magnetoresistance at room temperature in ferromagnetic thin film tunnel junctions,” *Phys. Rev. Lett.* **74**, 3273–3276 (1995).
- ³⁶ Y. Hou, F. Nichele, H. Chi, A. Lodesani, Y. Wu, M. F. Ritter, D. Z. Haxell, M. Davydova, S. Ilic, F. S. Bergeret, A. Kamra, L. Fu, P. A. Lee, and J. S. Moodera, “Ubiquitous superconducting diode effect in superconductor thin films,” *Phys. Rev. Lett.* **131**, 027001 (2023).
- ³⁷ H. Giil and J. Linder, “Superconductor-altermagnet memory functionality without stray fields,” *Phys. Rev. B* **109**, 134511 (2024).
- ³⁸ J. A. Ouassou, A. Brataas, and J. Linder, “dc Josephson effect in altermagnets,” *Phys. Rev. Lett.* **131**, 076003 (2023).
- ³⁹ C. W. J. Beenakker and T. Vakhtel, “Phase-shifted Andreev levels in an altermagnet Josephson junction,” *Phys. Rev. B* **108**, 075425 (2023).
- ⁴⁰ Q. Cheng and Q.-F. Sun, “Orientation-dependent Josephson effect in spin-singlet superconductor/altermagnet/spin-triplet superconductor junctions,” *Phys. Rev. B* **109**, 024517 (2024).
- ⁴¹ H. Reichlova, R. L. Seeger, R. González-Hernández, I. Kounta, R. Schlitz, D. Kriegner, P. Ritzinger, M. Lammell, M. Leiviskä, V. Petricek, P. Dolezal, E. Schmoranzarová, A. Thomas A. Bad’ura, V. Baltz, L. Michez, J. Sinova, S. T. B. Goennenwein, T. Jungwirth, and L. Šmejkal, “Macroscopic time reversal symmetry breaking arising from antiferromagnetic Zeeman effect,” arXiv:2012.15651v1 (2020).
- ⁴² R. Landauer, “Spatial variation of currents and fields due to localized scatterers in metallic conduction,” *IBM J. Res. Dev.* **1**, 223–231 (1957).

- ⁴³ M. Büttiker, Y. Imry, R. Landauer, and S. Pinhas, “Generalized many-channel conductance formula with application to small rings,” *Phys. Rev. B* **31**, 6207 (1985).
- ⁴⁴ G. E. Blonder, M. Tinkham, and T. M. Klapwijk, “Transition from metallic to tunneling regimes in superconducting microconstrictions: Excess current, charge imbalance, and supercurrent conversion,” *Phys. Rev. B* **25**, 4515 (1982).
- ⁴⁵ A. Soori, “Scattering in quantum wires and junctions of quantum wires with edge states of quantum spin Hall insulators,” *Solid State Commun.* **360**, 115034 (2023).
- ⁴⁶ A. Soori, S. Das, and S. Rao, “Magnetic-field-induced Fabry-Pérot resonances in helical edge states,” *Phys. Rev. B* **86**, 125312 (2012).
- ⁴⁷ W. Liang, M. Bockrath, D. Bozovic, J. H. Hafner, M. Tinkham, and H. Park, “Fabry-Perot interference in a nanotube electron waveguide,” *Nature* **411**, 665–669 (2001).
- ⁴⁸ A. Soori, “Transconductance as a probe of nonlocality of Majorana fermions,” *J. Phys.: Condens. Matter* **31**, 505301 (2019).
- ⁴⁹ S. K. Sahu and A. Soori, “Fabry-Pérot interference in Josephson junctions,” *Eur. Phys. J. B* **96**, 115 (2023).
- ⁵⁰ M. Papaj, “Andreev reflection at the altermagnet-superconductor interface,” *Phys. Rev. B* **108**, L060508 (2023).
- ⁵¹ M. Xu, Q. Q. Ge, R. Peng, Z. R. Ye, Juan Jiang, F. Chen, X. P. Shen, B. P. Xie, Y. Zhang, A. F. Wang, X. F. Wang, X. H. Chen, and D. L. Feng, “Evidence for an *s*-wave superconducting gap in $K_x\text{Fe}_{2-y}\text{Se}_2$ from angle-resolved photoemission,” *Phys. Rev. B* **85**, 220504 (2012).
- ⁵² X.-P. Wang, T. Qian, P. Richard, P. Zhang, J. Dong, H.-D. Wang, C.-H. Dong, M.-H. Fang, and H. Ding, “Strong nodeless pairing on separate electron fermi surface sheets in $(\text{Tl}, \text{K})\text{Fe}_{1.78}\text{Se}_2$ probed by arpes,” *Europhysics Letters* **93**, 57001 (2011).
- ⁵³ T. Qian, X.-P. Wang, W.-C. Jin, P. Zhang, P. Richard, G. Xu, X. Dai, Z. Fang, J.-G. Guo, X.-L. Chen, and H. Ding, “Absence of a holelike Fermi surface for the iron-based $\text{K}_{0.8}\text{Fe}_{1.7}\text{Se}_2$ superconductor revealed by angle-resolved photoemission spectroscopy,” *Phys. Rev. Lett.* **106**, 187001 (2011).
- ⁵⁴ Y. Zhang, L. X. Yang, M. Xu, Z. R. Ye, F. Chen, C. He, H. C. Xu, J. Jiang, B. P. Xie, J. J. Ying, X. F. Wang, X. H. Chen, J. P. Hu, M. Matsunami, S. Kimura, and D. L. Feng, “Nodeless superconducting gap in AxFe_2Se_2 ($\text{A}=\text{K}, \text{Cs}$) revealed by angle-resolved photoemission spectroscopy,” *Nature Materials* **10**, 273–277 (2011).
- ⁵⁵ D. Mou, S. Liu, X. Jia, J. He, Y. Peng, L. Zhao, L. Yu, G. Liu, S. He, X. Dong, J. Zhang, H. Wang, C. Dong, M. Fang, X. Wang, Q. Peng, Z. Wang, S. Zhang, F. Yang, Z. Xu, C. Chen, and X. J. Zhou, “Distinct Fermi surface topology and nodeless superconducting gap in a $(\text{Tl}_{0.58}\text{Rb}_{0.42})\text{Fe}_{1.72}\text{Se}_2$ superconductor,” *Phys. Rev. Lett.* **106**, 107001 (2011).